Transactions, **SMiRT-26**
Berlin/Potsdam, Germany, July 10-15, 2022
Division I

BRITTLE FAILURE ANALYSIS OF HIGH-BURNUP PWR FUEL CLADDING ALLOYS

Kai Simbruner[1], Michael C. Billone[2], Uwe Zencker[3], Yung Y. Liu[2] and Holger Völzke[3]

[1] Bundesanstalt für Materialforschung und -prüfung, Berlin, Germany (kai.simbruner@bam.de)
[2] PhD, Argonne National Laboratory (ANL), Lemont, USA
[3] Dr.-Ing., Bundesanstalt für Materialforschung und -prüfung (BAM), Berlin, Germany

ABSTRACT

The general aim of this research is the development of methods for predicting mechanical behavior and identification of limiting conditions to prevent brittle failure of high-burnup (HBU) pressure water reactor (PWR) fuel cladding alloys. A finite element (FE) model of the ring compression test (RCT) was created to analyze the failure behavior of zirconium-based alloys with radial hydrides during the RCT. An elastic-plastic material model describes the zirconium alloy. The stress-strain curve needed for the elastic-plastic material model was derived by inverse finite element analyses. Cohesive zone modeling is used to reproduce sudden load drops during RCT loading. Based on the failure mechanism in non-irradiated ZIRLO® claddings, a micro-mechanical model was developed that distinguishes between brittle failure along hydrides and ductile failure of the zirconium matrix. Two different cohesive laws representing these types of failure are present in the same cohesive interface. The key differences between these constitutive laws are the cohesive strength, the stress at which damage initiates, and the cohesive energy, which is the damage energy dissipated by the cohesive zone. Statistically generated matrix-hydride distributions were mapped onto the cohesive elements and simulations with focus on the first load drop were performed. Computational results are in good agreement with the RCT results conducted on high-burnup M5® samples. It could be shown that crack initiation and propagation strongly depend on the specific configuration of hydrides and matrix material in the fracture area.

INTRODUCTION

Zirconium-based alloys are a commonly used material for nuclear fuel cladding tubes. Pre-storage drying and the early stage of storage subject claddings to higher temperatures and pressure-induced tensile hoop stresses relative to in-reactor operation and pool storage. Under these conditions, radial zirconium hydrides may precipitate during slow cooling and degrade the cladding ductility due to their brittleness, cf. Motta et al. (2019). Application of mechanical loads may lead to a sudden loss of cladding integrity, cf. Billone et al. (2013). The hydride morphology plays an important role in the failure behavior, cf. Kim et al. (2015). Especially long, continuous radial hydride structures can cause severe embrittlement of claddings. The fuel rod may fail by fracture even at small deformations. A way to characterize the extent and morphology of radial hydrides is the radial hydride continuity factor (RHCF).

An established method for characterizing cladding material is the Ring Compression Test (RCT) where a small cylindrical sample of the cladding tube is subjected to a compressive load. This test is a laboratory representation of a fuel rod pinch load case and shows a high susceptibility to failure under the occurrence of radial hydrides. At Argonne National Laboratory (ANL), various quasi-static RCTs with high-burnup (HBU) pressure water reactor (PWR) fuel cladding alloys have been performed and the offset strain criterion for characterizing brittle failure of RCT samples has been established, cf. Billone (2011), Billone (2013).

Since the stress state during the RCT is not homogeneous, thorough finite element analyses (FEA) are necessary. Constitutive laws can be obtained by adjusting the stress-plastic strain curve in an inverse analysis approach, cf. Gomez et al. (2017a). In Martin et al. (2013) and Gomez et al. (2017b) it has been shown that the fracture of pre-hydrided cladding samples under RCT conditions can be reproduced by cohesive zone modeling. However, this model does not apply to fracture at small deformations during RCT.

In elastic fracture mechanics, the ability of a material to resist cracking is characterized by its fracture toughness; in elastic-plastic fracture mechanics the crack resistance is expressed by a *J*-integral initiation value as the most widely used concept. In case of cladding samples, due to the material behavior and the geometry, these concepts are not easily applicable. In Bertsch and Hoffelner (2006) a modified *J*-integral approach is presented, and crack-resistance curves were experimentally found on cladding samples without hydrogen. Cylindrical samples were fatigue pre-cracked and afterwards tensile loaded. Stable crack growth was documented along the axial direction of the cylinder. Nilsson et al. (2010) propose a FEA with fracture mechanics analysis. In that paper, hydrides are assumed as cracks inside the zirconium matrix and the *J*-integral is calculated for simple cases as well as various hydride morphologies.

At BAM (Bundesanstalt für Materialforschung und -prüfung), during the BRUZL project (Fracture mechanics analysis of spent fuel claddings during long-term dry interim storage), an approach of cohesive zone modeling was developed that can reproduce the interaction of radial hydrides and the zirconium matrix using a micromechanically inspired model. In this work, the developed methods are applied to samples of cladding alloy M5® that were subjected to a thermo-mechanical radial hydride treatment (RHT) to reorient existing circumferential hydrides to radial hydrides. A sample, that showed abrupt load drops during the RCT, was exemplarily selected and analyzed by means of fracture mechanics.

CLADDING MATERIAL

Sample preparation and the experimental procedure is documented in Billone et al. (2011). The investigated 8 mm sample ring 645D8 was taken from an 80 mm segment of a defueled M5® fuel rod cladding with burn-up of 63 GWd/MTU. To simulate drying conditions, RHT was applied. The pressurized and sealed segment was subjected a temperature of 400 °C and held for 1 h at that temperature with the target hoop stress being 140 MPa. The rodlet was slowly cooled at 5 °C/h to 200 °C while pressure and hoop stress were decreasing simultaneously. Below 200 °C, the cooling proceeded at higher cooling rates down to room temperature. The average hydrogen content measured at four different axial locations of the rodlet was 94 ± 6 wppm.

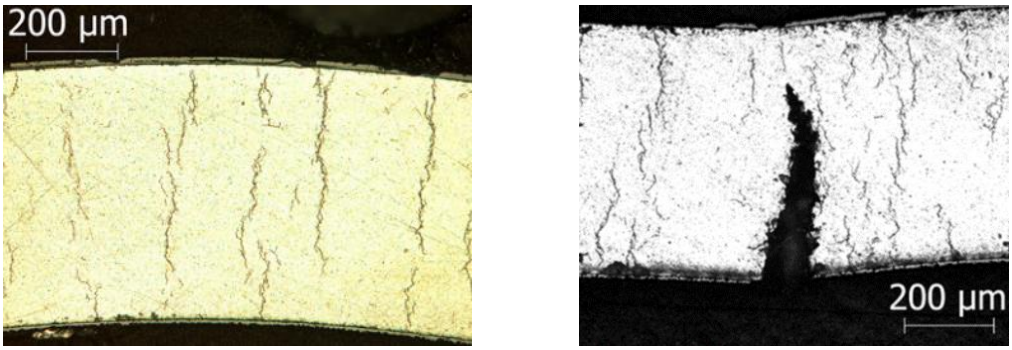

s

Figure 1. Micrograph of an HBU M5® cladding sample with 94 ± 6 wppm hydrogen after RHT (left). Major crack in HBU M5® after RHT and RCT (right).

An adjacent segment of the RCT-tested sample was used for metallographic studies. The cladding thickness was 0.55 mm, the corrosion layer thickness was 0.13 mm, and the total outer diameter of the cladding was 9.43 mm. Studies of the hydride morphology as depicted in Figure 1 (left) showed that more

than 95 % of the hydrides were oriented towards the radial direction with a RHCF being 50 ± 14 %. For the whole rodlet, an average RHCF value of 61 ± 18 % was specified.

RING COMPRESSION TEST

The test was conducted using an Instron 8511 servo-hydraulic material testing machine. Figure 2 (left) shows a photograph of the testing set-up with a cladding ring sample on top of the static support component, the load cell being located inside that static component, and the top plate being the loading plate. The test was performed at a temperature of 30 °C in displacement-controlled mode at constant loading of 5 mm/s until the maximum displacement of 1.7 mm. Then, the ring was unloaded at an unloading displacement rate of 5 mm/s.

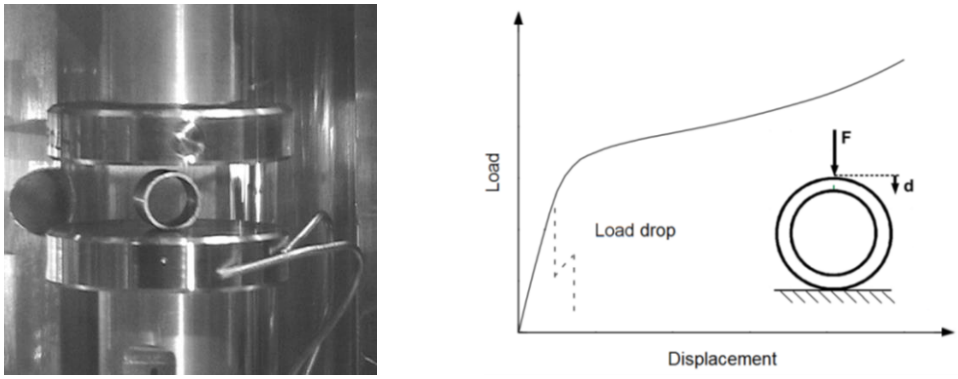

Figure 2. Testing machine Instron 8511 with ring sample (left) and schematic load-displacement behavior in RCT (right).

A schematic load-displacement curve of a RCT is shown in Figure 2 (right). The continuous line is an example of a test performed with a ring sample without radial hydrides. In contrast, the dashed line represents a load drop at the end of the linear portion. Such failure, as depicted in Figure 1 (right), usually occurs in claddings that feature distinct radial hydride structures as shown in Figure 1 (left).

FINITE ELEMENT ANALYSIS

To understand the complex interaction between hydrides and zirconium matrix, a FEA model was developed that can reproduce sudden load drops occurring during the RCT. Plane strain conditions were assumed. For all calculations, the commercial code ABAQUS® was used in quasi-static analysis mode. Mass inertia and the stiffness of the testing machine are large in comparison to the cladding sample. Hence, loading plate and static plate of the testing machine were modeled as analytical rigid parts. The solid section of the ring features plain strain elements with eight nodes, quadratic interpolation, and reduced integration (ABAQUS® element type CPE8R). At the 12 o'clock position of the ring, a gap of 1 µm width was modeled along 98,4 % of the wall thickness beginning at the inner surface. A cohesive section of the same thickness was inserted in that gap. Cohesive section and the surrounding mesh were connected via tie constraints. Two-dimensional cohesive elements with four nodes and linear interpolation were used (ABAQUS® element type COH2D4). All plain strain section lengths were set to match the sample length of 8 mm.

The simulation is displacement-controlled by the movement of the upper plate where also the ring loading is measured as the reacting force. All degrees of freedom of the lower plate were constrained as it represents the static component of the testing machine. ABAQUS® surface-to-surface contact was applied to model the contact between solid and rigid parts respectively. The tangential friction coefficient was set to 0.125 while the normal behavior was set to hard contact. Figure 3 (left) shows the generated finite element

mesh in its entirety and in detail around the cohesive zone (CZ). In the majority of the ring (between 1 and 11 o'clock positions) 12 elements are used over the wall thickness. Around the 12 o'clock position, where the CZ is located, the mesh was refined to account for the more complex stress state. The cohesive section itself was finely discretized to feature a single strip of 1000 cohesive elements.

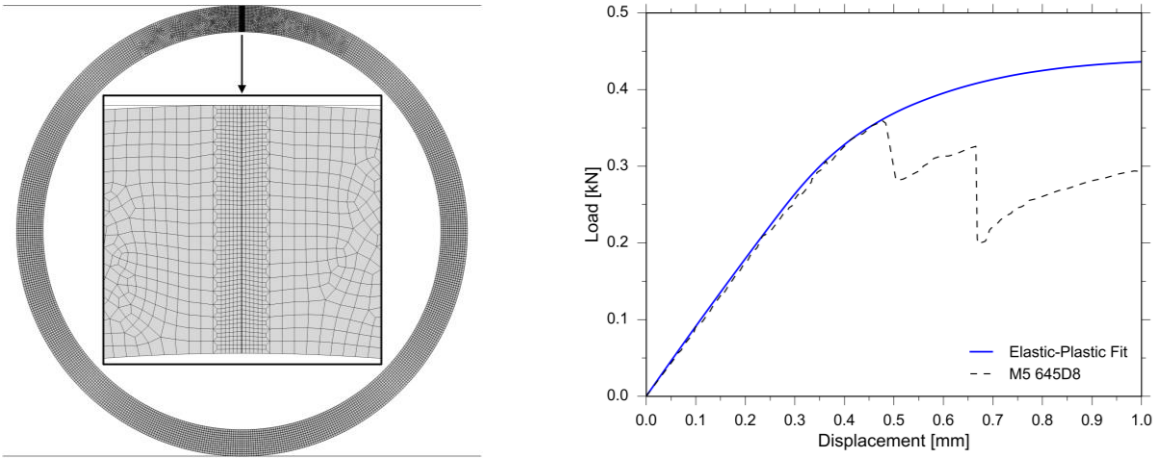

Figure 3. Mesh used in FEA of the RCT. A more detailed view of the CZ shows the mesh refinement around the cohesive elements (left). Load vs. displacement curve of a FE simulation without CZ (right).

Elastic-plastic material behavior was assumed for the solid section of the model. Values of Young's modulus E of 91.9 GPa from other sources, cf. Billone et al. (2021), were adjusted to 95.96 GPa to fit the elastic portion of the target experimental curve. Poisson's ratio ν is 0.37 for cold-worked recrystallized-annealed materials, taken from Billone et al. (2021). Assuming isotropy, a single stress-plastic strain relation can be obtained through inverse analysis studies, Gomez et al. (2017a). By comparing the deviation from a linear-elastic calculation and the experiment, the yield stress was determined to be 693.3 MPa. An excerpt of the tabular values is given in Table 1. If an experimental reference curve with a more prolonged ductile regime is available, the inverse analysis method can generate a relation that covers much higher plastic strains. However, the most crucial part of the load-displacement curve for samples that failed in a brittle fashion is just above the linear part of the curve. Therefore, very little plasticity is present, and a small number of data points yields good agreement between experimental and simulation results as shown in Figure 3 (right).

Table 1: Tabular values of the stress-plastic strain relation.

Stress [MPa]	693.3	702.9	704.5	710.3	737.8	753.0	756.7
Plastic strain [10^{-3}]	0	0.85	1.7	7.2	20.3	27.8	33.1

COHESIVE ZONE MODELING (CZM)

The constitutive law of the cohesive zone follows a traction-separation approach consisting of three parts: linear-elastic behavior, damage initiation, and damage evolution. Figure 4 (left) illustrates a typical traction-separation law. The material response in the elastic part, where the separation δ is smaller than a given value δ_1, is described by an elastic stiffness coefficient k. Young's modulus of the surrounding bulk material is divided by the initial thickness of the cohesive interface, which yields k= 95960 GPa/mm for the elastic stiffness of the cohesive interface. Damage is initiated inside a cohesive element as soon as an

applied tensile stress σ_c reaches the cohesive strength σ_{c0}. Any further separation δ of the element beyond δ_1 will monotonically increase its stiffness degradation, which is described by the scalar damage variable D, as defined by:

$$\sigma_c = k\,\delta\,(1 - D) \quad \text{with} \quad 0 \leq D \leq 1 \tag{1}$$

The evolution of the damage variable in dependency of $\delta - \delta_1$ in tabular form is required as ABAQUS® input parameter to define the cohesive law. When the separation reaches its maximum $\delta = \delta_3$, the corresponding cohesive element is removed from the analysis. The length of the upper section of the trapezoid is characterized by the ratio parameter:

$$r = \frac{\delta_2 - \delta_1}{\delta_3} \tag{2}$$

The energy dissipated in the damage process can be visualized as the surface under the traction-separation curve and is equivalent to the fracture energy release rate G_C. Since very little shear stresses are present in the fracture zone and the mode of failure is almost exclusively caused by tensile stress, which leads to separation of the cohesive interface in normal direction, a mode mix for the damage evolution was not considered.

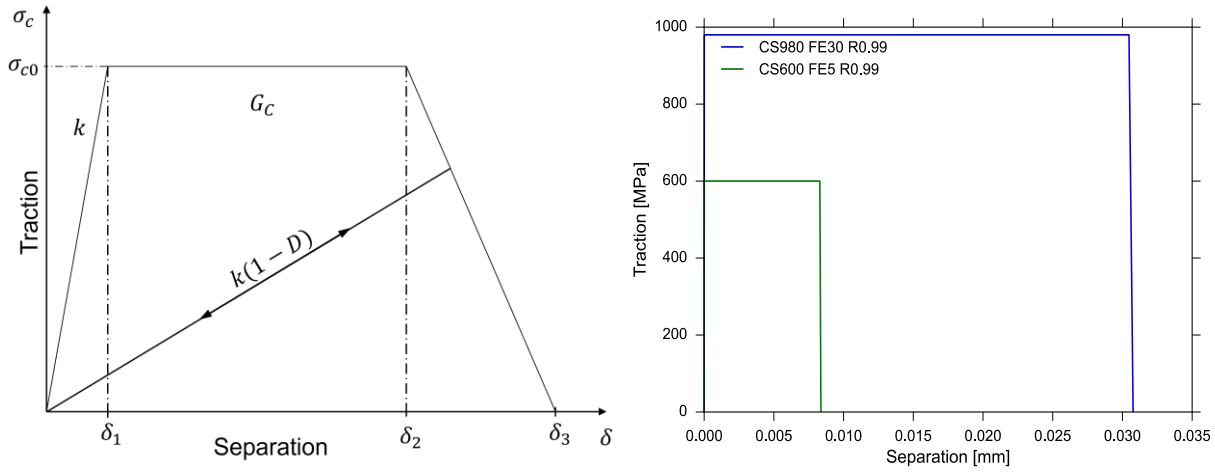

Figure 4. Schematic traction-separation response with trapezoidal damage evolution (left). Two different traction-separation responses implemented in the CZM (right). The matrix material (blue) has higher values of σ_{c0} and G_C than the hydrides (green).

The failure mechanism of cladding material with radial hydrides subjected to RCT conditions consists of two different types of failure, which can be examined by analyzing the fracture surface as shown in Figure 5 (left). Quasi-cleavage along hydride structures is the dominating type of fracture surface and an indicator of brittle failure, as described in Ruiz et al. (2021). However, some areas of the fracture surface show void growth and coalescence associated with ductile failure and crack propagation through the zirconium matrix. This surface composition was further investigated on non-irradiated, pre-hydrided RCT samples made of ZIRLO®, that were treated with similar RHT conditions (400 °C and 140 MPa hoop-stress) followed by RCT like the M5® sample investigated here. These studies revealed that 14.7 ± 5.2 % of the fracture surface, averaged over 10 scanning electron micrographs, show ductile behavior. The average length of these ductile patches projected in the direction of crack propagation is 17.4 ± 8.6 µm and their respective distance to each other is 65.6 ± 24.4 µm. This statistical model was implemented in a

PYTHON code to generate matrix-hydride distributions. A visualization of an exemplary result is shown in Figure 5 (right). Binary values, which either represent hydride (0) or matrix (1) properties, are assigned to the areas generated by the code and implemented in the FEA model via the PYTHON interface of ABAQUS®. This information is then projected onto the CZ and the two cohesive laws shown in Figure 4 (right) are assigned to the cohesive elements.

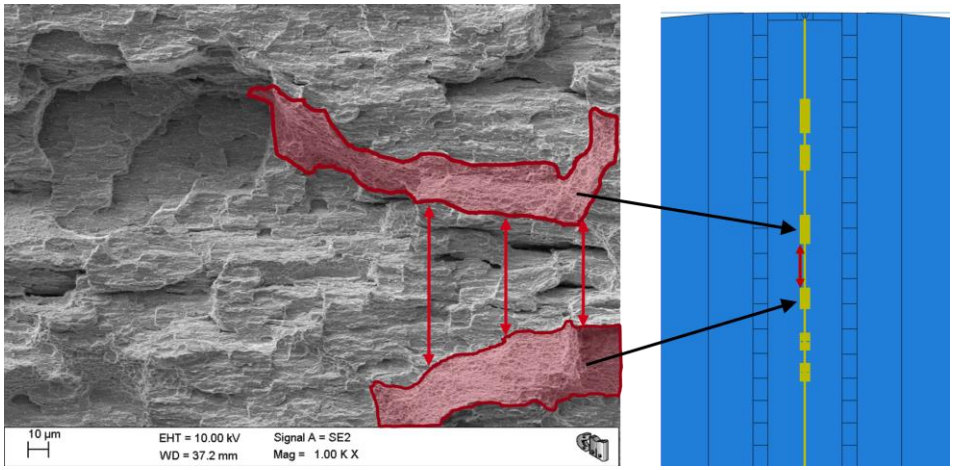

Figure 5. Scanning electron micrograph of a RCT sample fracture surface (left). The red areas show signs of ductile failure. The area fraction and geometry are transferred to the FEA model (right). Cohesive material parameters were assigned according to the distribution generated by this model.

The method as well as the cohesive laws were conducted from RCTs of the aforementioned ZIRLO® samples at room temperature and were used for all calculations in the current paper without alterations. However, adjustments were made to the matrix-hydride distribution to account for the different hydride morphology in M5® cladding material compared to the morphologies found in ZIRLO® claddings. The ductile surface fraction was set to 20 ± 5.2 % while an average length of 22 ± 8.6 µm and an average distance of 40 ± 24.4 µm were used.

FAILURE ANALYSIS

The load vs. displacement curves for the RCT of sample 645D8 and four representative results of the numerical simulations are shown in Figure 6 (right). In Figure 6 (left), the corresponding maximum principal stress state at displacement of 0.5 mm is given, where the load drop occurs in the experimental curve. The experimental protocol (Billone et al. (2011)) for sample 645D8 states, that the ring showed through-wall cracks at the 12 and 6 o'clock positions and a 90 % wall crack at the 8 o'clock position. The highest load prior to the first load drop was 0.360 kN at 0.5 mm displacement. With an offset strain of 0.7 %, the sample was classified as brittle according to the offset strain criterion, Billone et al. (2011).

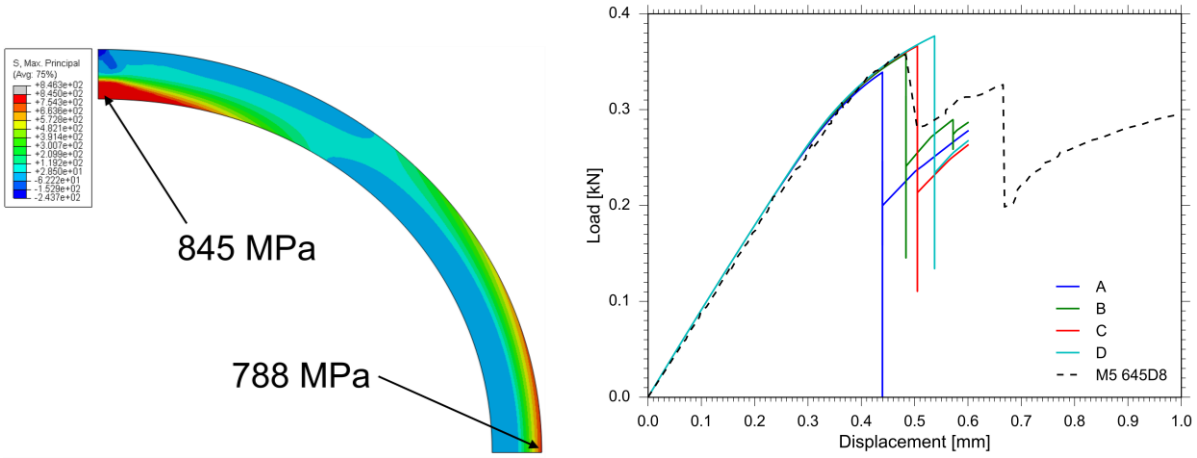

Figure 6. Maximum principal stress at 0.5 mm displacement during the RCT. The highest hoop stresses are highlighted (left). RCT results for the 645D8 sample (dashed line) and a selection of representative FE calculations (A, B, C, D) with varying distributions of matrix and hydride cohesive elements (right).

Analyzing the tensile stress state, the first crack is most likely to appear at the 12 or 6 o'clock position respectively. However, there is a steep stress gradient over the wall thickness. The areas closer to the outer diameter and the contact area with the loading plates are subjected to compression. With one or both inner diameter positions structurally weakened due to a crack, the stress state shifts and also favors subsequent cracking from the outer diameter at other positions than the 3 o'clock position as highlighted in Figure 6 (left). Because the exact order of fracture events is unknown, the 12 o'clock position at the inner diameter was chosen for the cohesive zone as the most susceptible spot. A total of 32 simulations with focus on the first load drop was performed. Therefore, the maximum displacement of 0.6 mm was chosen to save computational time. A new hydride distribution was generated for each run of the simulation without varying the statistical geometry parameters. There are short dips in load visible at every load drop. This behavior results from a large number of cohesive elements being removed from the analysis. Due to the massive loss of stiffness, the ring lifts off the loading plate where the load is measured, and the reacting force drops to zero momentarily. Other than the described behavior, there is no further impact on the simulation noticeable. The highest load prior to the load drop averaged over all simulations was 0.365 ± 0.011 kN, the correspondent average displacement was 0.5 ± 0.03 mm. These averaged values show good agreement with the experimental result and indicate a reasonable choice of cohesive zone parameters as well as geometric properties of the matrix-hydride distribution. The load drop of curve A occurred at the smallest load in this study. The load prior to the load drop was 0.339 kN at a 0.44 mm displacement. The matrix-hydride distribution applied for this specific simulation is shown in Figure 7 (left). In this depiction, the crack propagates from 0 to 1 along the normalized cohesive zone length, beginning from the inner 12 o'clock diameter of the ring. This distribution had a long segment of hydrides where the highest stresses occurred and therefore the crack initiated. Also, the first bridges of the stiffer, more resistant matrix material were rather small. In comparison, Figure 7 (right) shows the matrix-hydride distribution used for curve D. The load dropped at 0.377 kN and a 0.54 mm displacement. Two wide bridges of matrix material were located at the lower section of the cohesive zone, which provides a higher resistance against cracking.

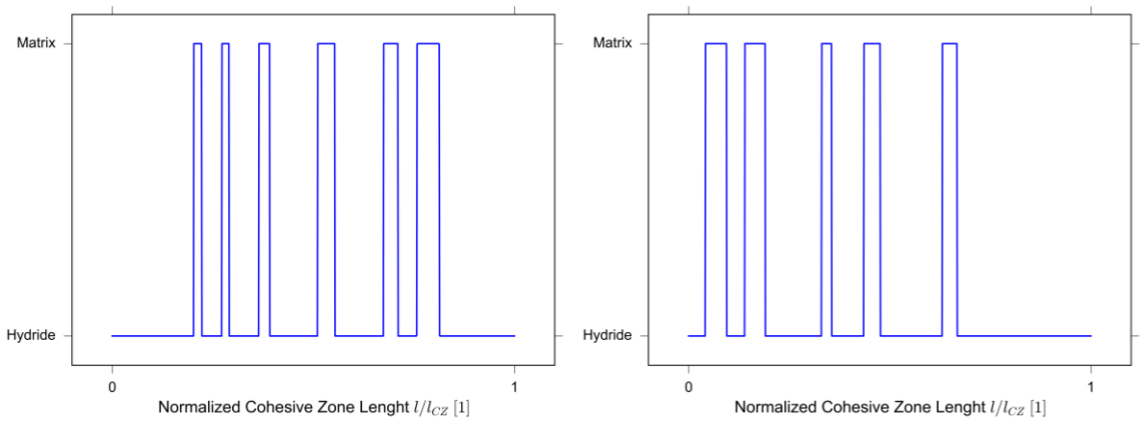

Figure 7. Matrix-hydride distributions in the cohesive zones of curves A (left) and D (right). The direction of crack propagation is from 0 to 1.

Since the experimental load drop is not as pronounced and sharp as the results of the FEA, both curves B and C and their respective load drops are in very close range of the experimental reference. Curve B had a load drop at 0.358 kN at a 0.48 mm displacement, curve C had a load drop at 0.366 kN at a 0.51 mm displacement. However, both curves show very different heights of load drops and re-loading behaviors with a smaller, subsequent drop on curve B. The matrix-hydride distributions for curves B (left) and C (right) are shown in Figure 8. Both distributions show similarities in position and width of the first three, most inward matrix bridges. In case of B, the initial, unstable crack growth was stopped by another matrix formation until becoming critical and causing a second load drop. On the other hand, the matrix-hydride distribution of C is more drawn towards the outer diameter. Hence, the unstable crack can propagate further resulting in a longer crack length and a flatter re-loading curve.

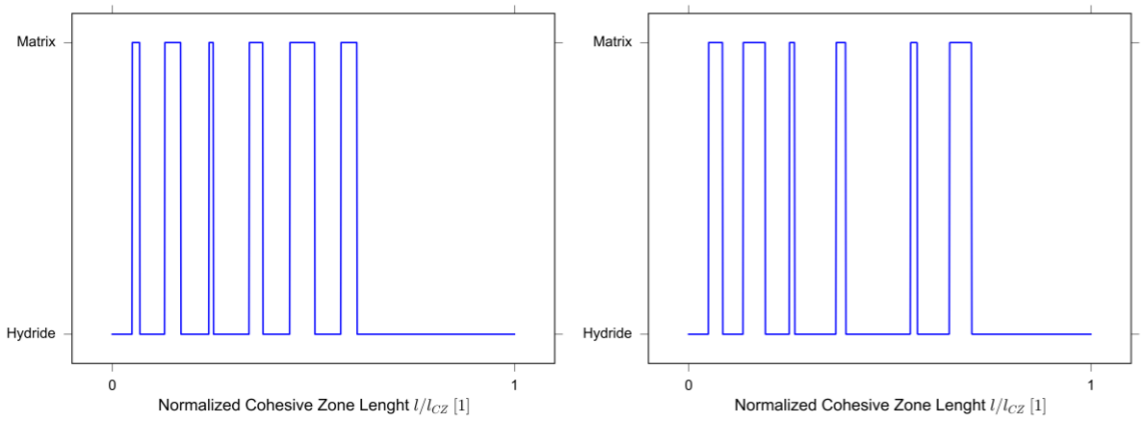

Figure 8. Matrix-hydride distributions in the cohesive zones of curves B (left) and C (right). The direction of crack propagation is from 0 to 1.

These four provided examples demonstrate the key findings of this study. Crack initiation is very sensitive with regard to the occurrence of ductile matrix segments at the inner diameter of the cladding at the 12 o'clock position. Even smaller, disconnected areas contribute to the resistance against cracking of

the structure as a whole. Once a crack is propagating, sufficient ductile patches in the center of the cladding can stop the crack growth and influence the final crack length.

CONCLUSION

A sample (8 mm length, total outer diameter of 9.43 mm, wall thickness of 0.55 mm) of HBU (63 GWd/MTU) M5® cladding with a hydrogen content of 94 ± 6 wppm was subjected to RHT. By sealing and pressurizing the rodlet, 140 MPa hoop stress were induced at the target temperature of 400 °C, held for 1 h, and subsequently cooled to 200 °C at 5 °C/h. The resulting RHCF was 61 ± 18 % with most hydrides reoriented in radial direction. RCT was conducted on the sample at 30 °C causing through-wall cracks at the 12 and 6 o'clock positions and a 90 % wall crack at the 8 o'clock position. The load-displacement curve of the RCT showed the first load drop at a displacement of 0.5 mm and was considered brittle by the offset strain criterion.

A FEA model of the RCT was presented. Assuming isotropic, elastic-plastic material behavior, elastic material parameters and a tabular stress-plastic strain behavior were fitted to the experimental reference curve of the M5® cladding sample. The failure behavior during the RCT was reproduced by implementing a cohesive zone at the 12 o'clock position of the FEA model. A micro-mechanical model was derived from analyzing scanning electron micrographs. The surface structure of a RCT sample fracture surface was mapped onto the cohesive zone. This allows for a modeling approach that supports two different types of failure in the same interface: brittle behavior along the hydrides and ductile behavior along the zirconium matrix. Each of the two types of failure is represented by a cohesive law. In agreement with the investigated micro-structure and the assumptions made regarding size, distance, and area fraction of matrix in the matrix-hydride distribution, a statistical model can compose cohesive zones for FEA. Combined with two cohesive laws for each the matrix material and the hydrides, sudden load drops at relatively small displacements under RCT loading can be reproduced by the computational model. The maximum load before crack initiation and the load drop calculated in the FEA is in good agreement with the experimental results.

It is important to point out the complex interactions between zirconium hydrides and the surrounding zirconium matrix in the fracture zone. It could be shown that even slight variations in the positioning of ductile patches in the fracture area can quantitatively and qualitatively alter the result of the RCT. For example, more or less load could be necessary to initiate a crack. The height of the load drop and the crack length respectively depend on possible matrix bridges in the center section of the wall thickness. Finally, even multiple load drops caused by consecutively initiating cracks at the same position of the ring are possible and could be reproduced.

ACKNOWLEDGEMENT

The authors wish to acknowledge the financial support of research project BRUZL (Fracture mechanics analysis of spent fuel claddings during long-term dry interim storage) by the German Federal Ministry for Economic Affairs (BMWi) under contract no. 1501561.

REFERENCES

Bertsch, J., Hoffelner, W. (2006). "Crack resistance curves determination of tube cladding material." *Journal of Nuclear Materials*, Elsevier, 352, 116-125.

Billone, M. C., Burtseva, T. A., Dobrzynski, J. P., McGann, D. P., Byrne, K., Han, Z. and Liu, Y. Y. (2011). "Used Fuel Disposition Campaign Phase I Ring Compression Testing of High-Burnup Cladding." Argonne National Laboratory report ANL-13/05, FCRD-USED-2012-000039, USA.

Billone, M. C., Burtseva, T. A., Chen, Y. and Han, Z. (2021). "Validation of Ductility Test Method and Criteria for Sibling Pin Cladding." Argonne National Laboratory report ANL-21/67, M2SF-21AN010201012, USA.

Billone, M. C., Burtseva, T. A. and Einziger, R. E. (2013). "Ductile-to-brittle transition temperature for high-burnup cladding alloys exposed to simulated drying-storage conditions." *Journal of Nuclear Materials*, Elsevier, 433, 431-448.

Gómez-Sánchez, F. J., Martin-Rengel, M.A. and Ruiz-Hervías, J. (2017a). "A new procedure to calculate the constitutive equation of nuclear fuel cladding from ring compression tests." *Progress in Nuclear Energy*, Elsevier, 97, 245-251.

Gómez-Sánchez, F. J., Martin-Rengel, M.A., Ruiz-Hervías, J. and Puerta, M. A. (2017b). "Study of the hoop fracture behaviour of nuclear fuel cladding from ring compression tests by means of non-linear optimization techniques." *Journal of Nuclear Materials*, Elsevier, 489, 150-157.

Kim, J.-S., Kim, T.-H., Kook, D.-H. and Kim, Y.-S. (2015). "Effects of hydride morphology on the embrittlement of Zircaloy-4 cladding." *Journal of Nuclear Materials*, Elsevier, 456, 235–245.

Martin-Rengel, M.A., Gómez-Sánchez, F. J., Ruiz-Hervías, J. and Caballero, L. (2013). "Determination of the hoop fracture properties of unirradiated hydrogen-charged nuclear fuel cladding from ring compression tests." *Journal of Nuclear Materials*, Elsevier, 436, 123-129.

Motta, A.T., Capolungo, L., Chen, L.-Q., Cinbiz, M.N., Daymond, M.R., Koss, D.A., Lacroix, E., Pastore, G., Simon, P.-C.A., Tonks, M.R., Wirth, B.D. and Zikry, M.A. (2019). "Hydrogen in zirconium alloys: A review." *Journal of Nuclear Materials*, Elsevier, 518, 440–460.

Nilsson, K.-F., Jakšic, N., and Vokál, V. (2010). "An elasto-plastic fracture mechanics based model for assessment of hydride embrittlement in zircaloy cladding tubes." *Journal of Nuclear Materials*, Elsevier, 396, 71-85.

Ruiz-Hervías, J, Simbruner, K., Cristobal-Beneyto, M., Perez-Gallego, D. and Zencker, U. (2021). "Failure mechanisms in unirradiated ZIRLO® cladding with radial hydrides." *Journal of Nuclear Materials*, Elsevier, 544, 152668.